Journal of Hydrology X 14 (2022) 100118

Contents lists available at ScienceDirect

Journal of Hydrology X

journal homepage: www.sciencedirect.com/journal/journal-of-hydrology-x

Research papers

Utility of low-cost recreational-grade echosounders in imaging and characterizing bubbly coastal submarine groundwater discharge

Mary Rose P. Gabuyo *, Fernando P. Siringan

The Marine Science Institute, University of the Philippines, Diliman, Quezon City 1101, Philippines

ARTICLE INFO

Keywords:
Submarine groundwater discharge
Low-cost
Single beam echosounder
Sidescan sonar
Mapping of SGD

ABSTRACT

Despite the growing knowledge on the significance of submarine groundwater discharge (SGD), mapping its occurrence is a continuing challenge. This study explores the capability and applicability of low-cost, off-the-shelf, recreational-grade echosounders (RGESs) to image different types and locate point sources of bubbly coastal SGD. Standard and systematic methodologies for efficient imaging and processing were established. The use of RGES was validated using a research-grade side scan sonar (RGSSS), continuous resistivity profiling, conductivity-temperature-depth casting, and MantaCam and SCUBA diving surveys. Lower frequencies (77/83 kHz) of RGESs showed more distinct acoustic signatures of bubbly SGD, as these were nearly the same as the effective resonance frequency of the bubbles. The clusters of bubbly discharges have higher backscatter strength than the water column noise, resulting in the definitive and convenient manual detection of SGD features. Hence, showing more accurate point sources of SGD. Three types of known SGD occurrence were identified and characterized based on acoustic behavior and spatial distribution: 1) sparse, discrete and sporadic discharge over wide area, 2) curtain, high and continuous bubble concentrations from widespread discharge, and 3) spring, direct bubble discharge from intense seafloor degassing at a single point source. These results showed that RGES provides a good alternative for more efficient and cost-effective preliminary coastal SGD works. Additional research on areas with water-dominated discharge but no bubbling is recommended.

1. Introduction

The need to address the difficulty in locating and assessing submarine groundwater discharge (SGD) by improving the mapping and measurement techniques has been continuously brought up in various work, particularly in coastal studies (Burnett et al., 2001; Burnett et al., 2006; Kang et al., 2019; Moore, 2010; Moosdorf et al., 2015; Prakash et al., 2018; Taniguchi et al., 2019).

In this study, SGD represents all direct discharge of subsurface fluids (e.g., submarine fresh groundwater, recirculated saline water, and CO_2 and CH_4 gases) across the seafloor (Fig. 1), from the intertidal zone to deep-sea (Burnett et al., 2001; Burnett et al., 2003; Taniguchi et al., 2002). Generally, the most prevalent freshwater SGD is found closest to the shore. Whereas gas bubbles are common indicators of SGD seeping from the seafloor in hydrothermal and hydrocarbon areas (Burnett et al., 2006; Nakamura et al., 2015; Cardenas et al., 2020). The release of the bubbles in hydrothermal areas are driven by the volcanic degassing of CO_2 (Cardenas et al., 2020), while in hydrocarbon areas it can be a result of the decompression of CH_4 which can be produced by the intensive freshwater-driven methanogenesis (Idczak et al., 2020).

In any coastal region, SGD is ubiquitous and may take different physical forms (Burnett et al., 2001; Moore, 2010; Mulligan et al., 2019). Low and small upward leakages over wide areas are prevalent in permeable sediments, whereas intensely channelized and focused small springs are seen in impermeable regions cut by conduits (i.e., cavities in karsts, bedding planes, and faults in solid bedrocks), where they enter the sea as submerged springs (Burnett et al., 2001; UNESCO, 2004).

Contrary to earlier knowledge that this phenomenon was insignificant and can be unremarkable as it flows much slower than surface runoff (Mulligan et al., 2019), studies have shown that it can be widespread and, in some areas, have greater ecological significance (Johannes, 1980; Senal et al., 2011). However, SGD remains difficult to detect and quantify, resulting to ambiguities in understanding subsurface processes (Taniguchi et al., 2006).

Among the commonly used methods for identifying and mapping SGD include tracer techniques using Radon-222 and Radium-223/224 and electrical resistivity profiling (Taniguchi et al., 2019). These techniques continue to evolve through time due to the recognition of

* Corresponding author.
E-mail addresses: mgabuyo@msi.upd.edu.ph (M.R.P. Gabuyo), fpsiringan@msi.upd.edu.ph (F.P. Siringan).

https://doi.org/10.1016/j.hydroa.2021.100118
Received 13 August 2021; Received in revised form 20 December 2021; Accepted 22 December 2021
Available online 29 December 2021

limitation from generalized assumptions and natural variability (Szymczycha and Pempkowiak, 2016).

In more recent years, geophysical methods using hydroacoustic tools such as echosounders are explored for mapping and imaging sea features and phenomenon which can be related to, or can indicate occurrence of SGD (e.g., submarine volcanoes, gas hydrates or bubbles). However, reports are concentrated in deep open-ocean investigations, usually linked to surveys for hydrocarbon and petroleum deposits, and submarine volcanoes (Baraza and Ercilla, 1996; McCartney and Bary, 1965; Mitchell et al., 2017; Tsai et al., 2017).

Echosounders collect two types of data: seafloor depth/bathymetry and backscatter. Bathymetry is measured using the time it takes for the sound to be transmitted back to the receiver, whereas backscatter is the amount of sound reflected to the receiver (Medwin and Clay, 1998; NOAA, 2019). Gas bubbles and freshwater discharge in seawater can act as strong acoustic scatterers, due to differences in density, speed of sound between the different media/layers in the water column, and the resonance effect (Medwin and Clay, 1998; Nakamura et al., 2015). The resonance effect is controlled by the size of the bubble, frequency, and water depth (Nakamura et al., 2015). Echosounders are single beam systems (i.e., fish finders), side scan sonars, and multibeam echosounders (Medwin and Clay, 1998).

In this study, the recreational-grade echosounder (RGES) is a single beam system now commonly used in recreational activities such as sports fishing. RGES was the tool of choice for seafloor mapping before the multibeam systems became more accessible in the 1980's (Blondel, 2009).

In a survey intended to map active offshore faults in an area known to have bubbly SGD, an RGES with side scan imaging capability captured the bubble discharges in the water column of the coastal areas of Mabini and Tingloy, Batangas. Following this discovery, this study explored the capability and applicability of RGES in locating bubbly SGDs and identifying point sources to depths of about 50 m in areas with previously documented occurrences.

Use of RGES may provide a faster and cost-efficient preliminary identification and mapping of sites with bubbly SGDs, narrowing down areas for further investigation. Availability of SGD maps may help in enhanced understanding of the phenomenon and its influence on the ecosystem.

2. Materials and methodology

Standard and systematic methodology for efficient imaging and processing using RGES was established in this study. The datasets were acquired from 2017 to 2020. The workability of the RGES with fixed frequencies as a low-cost alternative method in imaging and characterizing SGD occurrence and locating point source was assessed. The utility of the RGES was validated using a research-grade side scan sonar (RGSSS), and through continuous resistivity profiling (CRP). The RGSSS is more commonly used in scientific studies due to its large area coverage and high-resolution seafloor images that are comparable to the quality and extent of satellite images (Blondel, 2009). To help in the validation of occurrence of bubbly SGDs, underwater photographs were also collected using MantaCam, a towed video imaging system, and during SCUBA diving for ground-truthing.

2.1. Research area

The study sites are in Mabini and Tingloy, Batangas, Southern Luzon, Philippines, where different types of SGDs related to hydrothermal activities are known to occur (Fig. 2). SGD sites are known dive sites frequented by tourists. SGDs in these areas were previously determined via small, diver-based surveys and radon measurements in zones with evident bubbling, and varying temperature (Cardenas et al., 2020). Cardenas et al. (2020) looked at pCO_2 to identify areas of high degassing, whereas Rodolfo (2019) measured the distribution of Radon-222 to identify areas of high SGD.

The study areas lie within the Verde Island Passage Marine Corridor (VIPMC), a volcanic region with an active hydrothermal system. It is characterized by tectonic structures such as NE-SW trending gravity faults and SW trending volcanic ridges which resulted from the active subduction along the southern segment of the Manila Trench (Del Rosario and Oanes, 2010). The nearest highly active volcano in the area is Mt. Taal (Fig. 2), a 311-m high complex volcano (Cardenas et al., 2020) which had its most recent phreatomagmatic explosion in January 2020.

The region is also recognized as a significant conservation area due to several endangered to critically endangered species of mammals and turtles, in addition to the significantly high coral and reef fish diversity (Horigue and Licuanan, 2013). With a high concentration of species per unit area, VIPMC is identified as "the center of the center of marine shore fish biodiversity" (Carpenter and Springer, 2005).

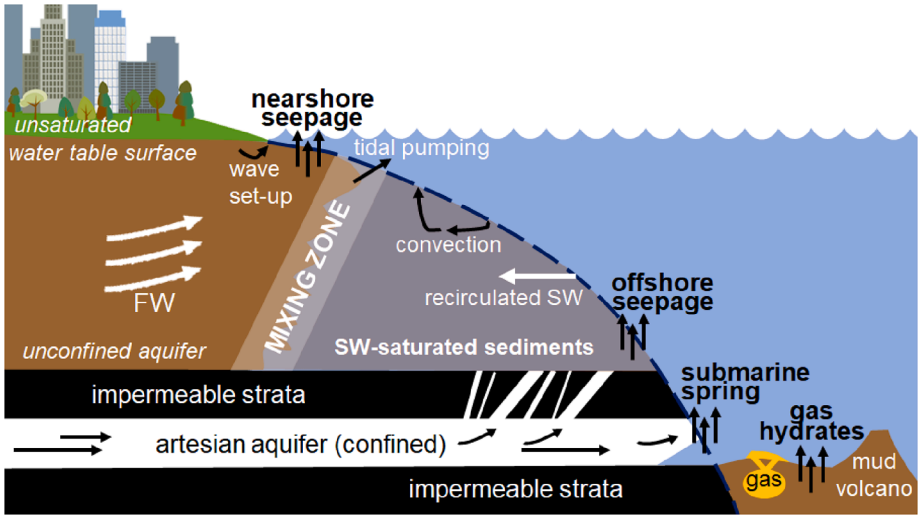

Fig. 1. Diagram of groundwater and submarine groundwater discharge flow. Different types of SGD occurrences are shown – nearshore seepage, offshore seepage, submarine springs, and gas hydrates. FW = freshwater; SW = saltwater. (Modified from Burnett et al. (2001), and Taniguchi et al. (2002).

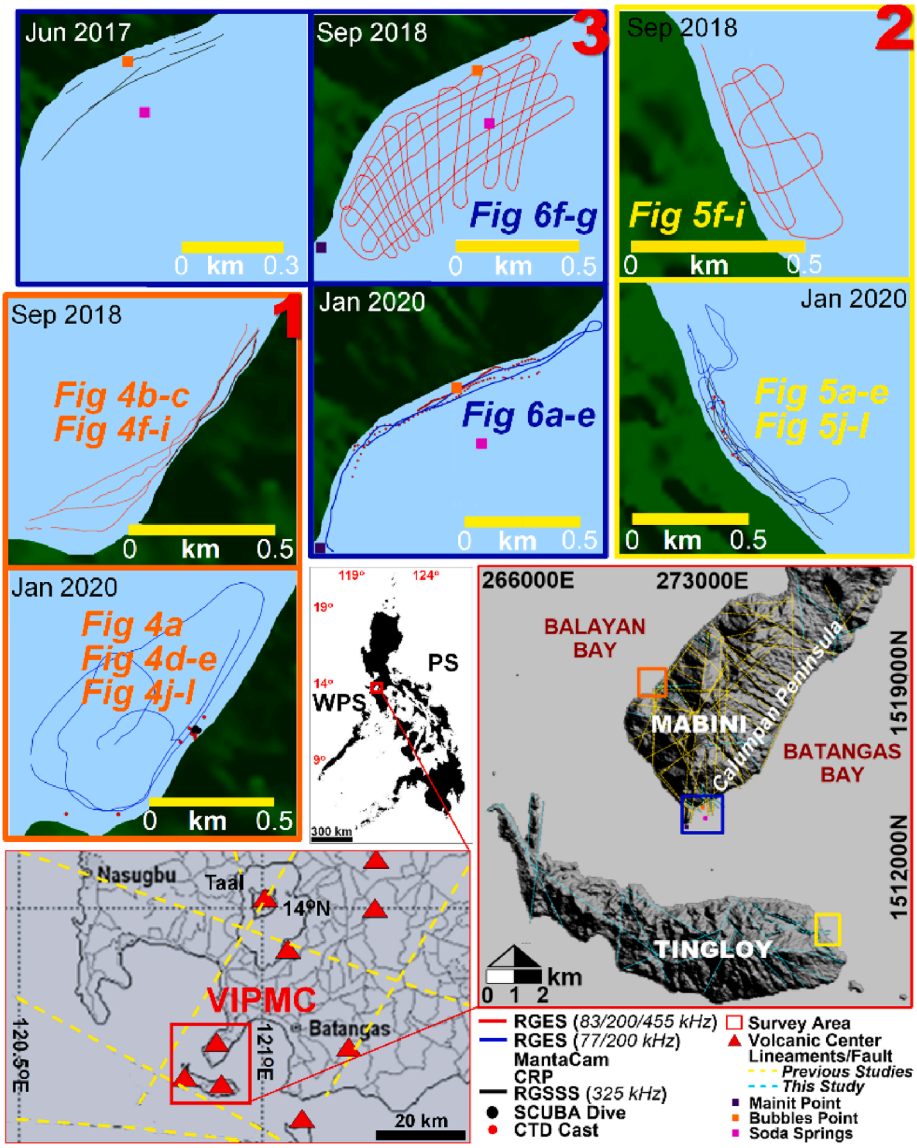

Fig. 2. Map of the study sites, with corresponding survey tracks and site plots. Survey areas include the previously identified SGD occurrences in the Verde Island Passage Marine Corridor (VIPMC): 1) Balayan Bay (sparse-type), 2) Tingloy (spring-type), and 3) Batangas Bay (curtain-type). WPS: West Philippine Sea, PS: Philippine Sea. For reference, figures presented in the Results and Discussion are labelled accordingly in the maps. Lineaments in VIPMC map are from Del Rosario and Oanes (2010).

2.2. Recreational-grade echosounder (RGES)

2.2.1. Equipment and equipment set-up

Two RGES were used: 1) Humminbird 698ci HD SI Combo (or Humminbird), a compact unit with a side scan capability that belongs to a wide array of portable systems by Humminbird, and 2) Garmin echoMAP 50s (or Garmin), a unit that belongs to the Garmin series of chart plotter and fish finder combination.

The RGESs collect the same type of data as typical echosounder systems but are more streamlined and designed for ease of use (Kingon, 2013). Both units are composed of a small transducer that can be deployed on the side of a vessel with a pole, 12-volt power cable, a 12-volt power bank, and a compact main control head unit (Fig. 3). Since the RGESs are primarily manufactured as location tracker and depth meter, GPS coordinates and tracks, and water depths were also recorded.

The side beams of the Humminbird operate at a frequency of 455 kHz, with a DualBeam PLUS™ sonar coverage at 200/83 kHz (Humminbird, 2013). Dual-beam transducers use multiple elements aimed at different directions and angles to maximize the coverage capacity. For areas at the bottom of the boat, the down scan beam is transmitted (Humminbird, 2013). The side scan sonar's maximum slant range is about 120 m for each side, with a bottom coverage diameter of about

Fig. 3. Humminbird 698ci HD SI Combo primary components and set-up: (a) Main control head unit is connected via (b) 12-volt power cable to a (c) 12-volt power bank. The control head is also connected to a (d) small transducer that is side-mounted at/near the center-of-gravity of the outrigger boat with a (e) 1.8 m pole. (Notes: The safety rope from the transducer to the boat aids in stabilization of the transducer as it moves through the water during surveys. Whereas the control head unit is placed as near as possible to the transducer for more accurate, real-time measurements and recordings.)

twice the depth, and maximum depth capacity of about 50 m. Whereas the 83 and 200 kHz down frequencies are transmitted as 60° and 20° conical beams, respectively (Humminbird, 2013).

For Garmin, the transducer uses a conical beam with a coverage of 45°/15° for the 77/200 kHz dual-beam frequency, with a maximum depth capability of about 210 m (Garmin, 2016).

The bottom coverage area of the conical down beams for both units mainly depends on the cone angle, sonar frequency, water depth, contour, and presence of scatterers (Homestead, 2017). In general, since lower-frequency sound waves have wider cone angles, they also have wider cone bases, capturing more features at a time. The diameter (d) of these footprints can be theoretically determined by the following formula, where D is the water depth and θ is the beam width (Humminbird, 2013):

$$\mathbf{d} = 2\mathbf{D}^{*}\mathbf{tan}(\theta/2)$$

Hence, 77 kHz has a cone base diameter equal to about three-fourths of the depth, 83 kHz covers a base area with a diameter that is approximately equal to the depth, whereas 200 kHz cone has a diameter that is about one-third of the depth (Humminbird, 2013).

The sensitivity of Humminbird to backscatter acquisition was set to a conservative level (12 from the scale of 0 – 20) to avoid noises (e.g., sounds from micro/macroorganisms, wave bubbles, nepheloid, and suspended sediments/materials). Whereas for Garmin, sonar gain and color intensity were set to low - medium sensitivity sonar returns to disregard these noises.

2.2.2. Survey design and operation

An outrigger boat (at least 5 m long and 1 m wide), a design that minimizes roll, was used for the surveys. The transducers were side-mounted within the fulcrum area of the boat to minimize errors due to pitch. The transducers were placed at a depth just below the keel (i.e., ~0.3 m) to avoid signal interference from the boat (Fig. 3). As much as possible, the boat ran along a straight line (with minimal turns to prevent distortion and smearing of the image) or parallel to the coast, at 1 kt to 2 kts (depending on the wave and wind conditions). Perpendicular survey tracks were also added to acquire more information on target shape.

2.2.3. Data processing and analysis

For Humminbird, the recorded data included the sonar images acquired using side scan and down scan (455 kHz) and dual-beam (83/200 kHz), with the GPS tracks and corresponding water depths. The extracted sonar recording files include different file extension formats. In this study, only the SONAR (.son), and DATA (.dat) files were used. The .dat files were viewed and analyzed using the main processing software used in this study, HumViewer, a freeware used to view and analyze sonar recordings acquired by Humminbird sonar imaging units. Installation of this software only requires, at the minimum, Java version 1.6, 32-bit Windows, and screen resolution down to 1024 × 768.

Sonar recording files with identified bubbly SGD signatures were selected and analyzed using this software. For presentation purposes, the selected images were further refined and annotated using free image post-processing software, GNU Image Manipulation Program (GIMP 2.10.20). HumViewer can be connected to Google Earth, where the GPS tracks were plotted and saved as .kml. The saved track file was then opened in QGIS to plot the locations of SGD occurrences in sonar images on a separate base map. For the bathymetry data, the saved track data were downloaded using HumminbirdPC. The points were converted to .csv using MS Excel, and further converted to charts (.grd) using Surfer 11. The .grd file was viewed and transformed into a bathymetric chart using QGIS.

Whereas for Garmin, the extracted sonar recording files were saved in binary file format (.RSD), and GPS positions were recorded as Garmin UserData (.AMD). Garmin datasets were viewed and analyzed using Garmin HomePort, a map-viewing and GIS software primarily used for all data acquired using any Garmin GPS navigation devices.

In some of the 200 kHz sonar images of Garmin, the rise velocities of the bubbles were estimated to approximate the size of the rising bubbles using the well-defined bubble lines of the identified SGD features. These bubble lines are formed as the vessel drifted across the survey area, leaving linear acoustic anomalies of rising bubbles within the bubble cluster (Greinert, 2008). The varying slopes of the bubble lines indicate different rise velocities (Hernández et al., 2017). Rise velocities were then estimated from the time difference between two distinct depths along the same bubble line (Artemov, 2006) using the Measure tool in HomePort. Extracted depth data (i.e., .xyz files) were converted to .grd using Surfer 11. The .grd files were then viewed using QGIS as Hillshade bathymetry.

2.3. Confirmatory surveys

2.3.1. Research-grade side scan sonar (RGSSS)

The applicability of a research-grade side scan sonar (RGSSS) in coastal SGD imaging was also established from previous field activities while imaging coral reefs in Anilao, Batangas. Sonar images from the RGSSS were used to validate the resulting images of the RGES.

The RGSSS used is the C-Max CM2 system. This unit is composed of digital CHIRP towfish, sonar transceiver (STR) topside unit, MaxView acquisition software with a dongle installed in a ruggedized laptop, coaxial hand-hauled tow cable, and 12-volt deep cycle battery connected to a power inverter with 220-volt output.

The towfish has two different frequencies: 325 kHz and 780 kHz, with maximum ranges of 200 m/side and 50 m/side, respectively. It weighs 18 kg in air and 11 kg in water. Whereas the transceiver is a compact, rugged, splashproof topside unit with a plug-and-play USB connection to the MaxView acquisition software. The towfish was towed at the side of an outrigger boat, near the center-of-gravity, while the control head unit was placed as near as possible to the towfish.

The boat ran at 2 kts to 4 kts. For this survey, only the 325 kHz was used as it was the effective frequency for this type of work, based on the previous surveys conducted. Overlap and orthogonal survey tracks were traversed for best target detection probability. The sonar recordings acquired was in CM2 Side scan Record format. The files were converted to .xtf using MaxView, the same software used during the survey. The converted image files were uploaded to Hypack 2015 for processing, mosaicking, and analyzing. Generated images were exported as .tiff images. These images were readily overlain to the base map uploaded in the same software. Post-processing of the image (i.e., annotations) was done using Surfer 11.

2.3.2. Continuous resistivity profiling (CRP)

The AGI SuperSting R8 resistivity meter was used for CRP. The electrode array was towed at the water surface behind the boat, at a speed of about 2 kts. The CRP unit simultaneously collected GPS position and depth from a separate sonar transducer (i.e., water depth). Only 24 electrodes were used because of the shallow depth and limited turning capability due to busy sea traffic. A floater was tied to the end of the cable to exert a drag and straighten the cable line. A sinker was placed two dead electrodes closer to the boat to prevent the lead electrodes from emerging above the water during the survey. The surveys were conducted in the early morning (i.e., 6:00 AM – 9:00 AM) to be consistent with most of the sonar surveys and to avoid the time when divers are in the water. For this survey, a bigger outrigger boat was needed (i.e., 10 m long and at least 1 m wide) since the equipment components are bulky and heavy.

The acquired .stg data were viewed and processed using AGI EarthImager, a licensed software which subscription came along with the system package. To successfully process the data, the GPS and depth data from the external echo sounder must match all measurements, otherwise, processing error will occur.

The interpretation of the electrical resistivity (ER) data followed the

assumptions presented by Cantarero et al. (2019): 1) negligible lithologic influence, 2) absence of conductive materials along the survey lines, and 3) porewater conductivity controls the bulk resistivity. This study also used the same limits from Cantarero et al. (2019) for the classification of the resistivity units: fresh groundwater (ER $>$ 3 Ω-m), mixed waters (1 Ω-m $\leq$ ER $\geq$ 3 Ω-m), and seawater/saline groundwater (ER $\leq$ 1 Ω-m).

2.3.3. Conductivity-temperature-depth (CTD) casting

A Seabird 19plus V2 CTD-submersible pump flow-through system was used to directly profile salinity and temperature in the sites. CTD casting was conducted for characterization of the water column and correlation with the acoustic images. Three CTD data were considered relevant to this study: salinity, temperature, and conductivity. Seawater is saturated with salts, from 28 psu to 41 psu (TMCS, 2019). Temperature commonly ranges from −2°C to 28 °C but are hotter in hydrothermal vents or closer to land (TMCS, 2019). Seawater conductivity is naturally at 5.5 S/m, whereas freshwater stream conductivity ranges from 0.05 S/m to 2 S/m (FEI, 2014).

Water flow has a significant effect on these values. Freshwater input naturally decreases salinity and conductivity values, unless the inflow is a highly mineralized groundwater inflow which results to elevated values due to the presence of more ions (FEI, 2014).

CTD casting was done manually, in two different ways: 1) Purposive CTD casting, the unit was lowered inside and outside the identified bubble fields, with GPS position of each cast recorded using a handheld GPS device; 2) Yoyo method, the unit was continuously lowered and raised as the boat ran at a speed of about 2 kts along a track, with a handheld GPS recording the points where the unit was lowered.

CTD data were saved as .HEX files, generated through SeaTerm and processed using SBE Data Processing software developed by Seabird. The dataset were converted to .ASCII format in this software. ASCII files were then converted to .csv for further analysis using MS Excel.

2.3.4. MantaCam imaging and SCUBA diving

MantaCam is a rapid reef mosaicking tool that can make fast and frequent surveys of submarine environments. The concept design of the unit is similar to the Teardrop Tow (Judilla et al., 2012). The unit is composed of a V-shaped flat stainless steel that holds a waterproof digital camera (e.g., GoPro) in video mode while being towed by a boat over the survey area. MantaCam is limited to imaging of seafloor at shallow depths due to light limitations, with survey time between 8:00 AM and 4:00 PM when sunlight is enough for video capture. For this study, the device was tied to the side of the boat, towed at a speed of about 2 kts. The acquired videos were viewed using VLC Player. Screenshots of relevant frames were taken and further annotated using Surfer 11.

SCUBA diving was conducted in selected sites for up-close observation of the visible expression of SGD (e.g., bubbling). For areas with obvious and significant bubbling, observations (e.g., size, density/dispersal) of the bubbles from the origin at the seafloor were noted. Additional photographs of the relevant features were taken using underwater cameras. Photographs from both methods were used for the primary ground-truthing to show the actual occurrence of bubbly SGD in the sites.

3. Results and discussion

The workability of an RGES in imaging bubbly SGD occurrence and locating point source was assessed using the acquired sonar images. Results were confirmed with the sonar images acquired using RGSSS, resistivity profiles from CRP, parameter measurements from CTD casting, and photographs from MantaCam and SCUBA diving activities.

The RGESs used are mainly built for leisure. But from the results, the units can effectively generate good-quality sonar images that can be used to locate, map, and characterize previously known bubbly SGD occurrences in the study sites. Three types of SGD occurrence were identified based on their acoustic behavior and spatial distribution: 1) sparse-type (i.e., Balayan Bay), 2) spring-type (i.e., eastern coast of Tingloy), and 3) curtain-type (i.e., Batangas Bay).

Sparse-type referred to discrete SGD occurrence sporadically distributed over a limited area. Spring-type was discrete and direct discharge caused by intense degassing from a single point source at the seafloor. Curtain-type described high concentrations of bubbles from widespread and extensive seafloor degassing.

3.1. Sparse-type

In Balayan Bay, SGD occurs as a discrete field of continuously rising, warm, bubbly discharges with varying bubble sizes (i.e., $<$5 mm at point sources to $>$30 mm at surface). These features were observed during the dive less than a meter away from the coast, at depths $<$1 m to about 12 m, rising from the seafloor covered with boulders, live corals, and coral rubble. Depths shallower than 5 m had more frequent gas discharges (Fig. 4a). Beyond 5 m, bubbles were sporadic (4b). For a copy of the SCUBA dive video, follow this link: https://tinyurl.com/balayanSGD.

Upon confirmation from the dive, these features were then imaged using the RGSSS with 325 kHz frequency. Signatures of known SGD were indistinct acoustic anomalies in the water column, at depths of about 1 m to 15 m (4c and 4d). Gas bubbles were imaged as sporadic near-seafloor or mid-water features along the 50-m transect (4d) of the 120-m traverse (4c). Other features imaged were corals and coral rubble covering the seafloor, and the track of the boat (nadir zone).

The RGES units also imaged these features. In all images (4e – 4j), the brighter signatures in the water column indicate high scattering/high concentrations, whereas darker colors reflect low concentrations/low scattering. Fig. 4e and 4f show the sparse-type SGD at depths of about 8 m to 12 m imaged using Garmin. The sonar images show 15-m thick and discrete, vertically rising bubbles. In 77 kHz, the identified SGD signature (4e) was more extensive, with stronger signal than in 200 kHz (4f).

Fig. 4g to 4i show the processed sonar images acquired with Humminbird at $<$ 1 to 5 m depth. SGD was indicated by 54-m isolated, near-seafloor to mid-water, rising bubbles with no significant change in the stream width across the water column. Images from down scan frequencies 83 kHz (4h) and 200 kHz (4j) show more distinct occurrence with more discernable signal from the background noise compared with the down scan sonar image of 455 kHz (4i).

Aside from SGD, other features were also imaged although considered noise in this study. In all frequencies, signals which may indicate the wake of a passing boat, suspended sediments, or bubbles due to air-sea interactions were seen in the water column. Features which look like part of the benthos (yellow arrows in 4h, 4i and 4j) were also imaged. In the down scan image of 455 kHz (4i), these features are not as persistent as seen in the two lower frequencies. Both side scan and down scan of 455 kHz also imaged the rough, coralline seafloor morphology of the area.

CRP result indicated that in near-surface sub-bottom depths down to 24 m, high resistivity corresponds to the location of these bubbles. The resistivity values indicate the presence of brackish waters in the subsurface, further suggesting recirculation of seawater. From CTD casting, locations of the identified sparse-type SGD features correspond to areas with low salinity (4k), low temperature (4l), and low conductivity (4m) values compared to ambient nearshore conditions, further confirming that the bubbles imaged using RGES indicate SGD occurrence. However, both temperature and conductivity were decreasing with depth, whereas salinity was increasing with depth. A nearby river drains near the bubble field, which may have contributed to the relatively low temperature and salinity values at the surface.

3.2. Spring-type

In the eastern coast of Tingloy, spring-type SGD features were seen

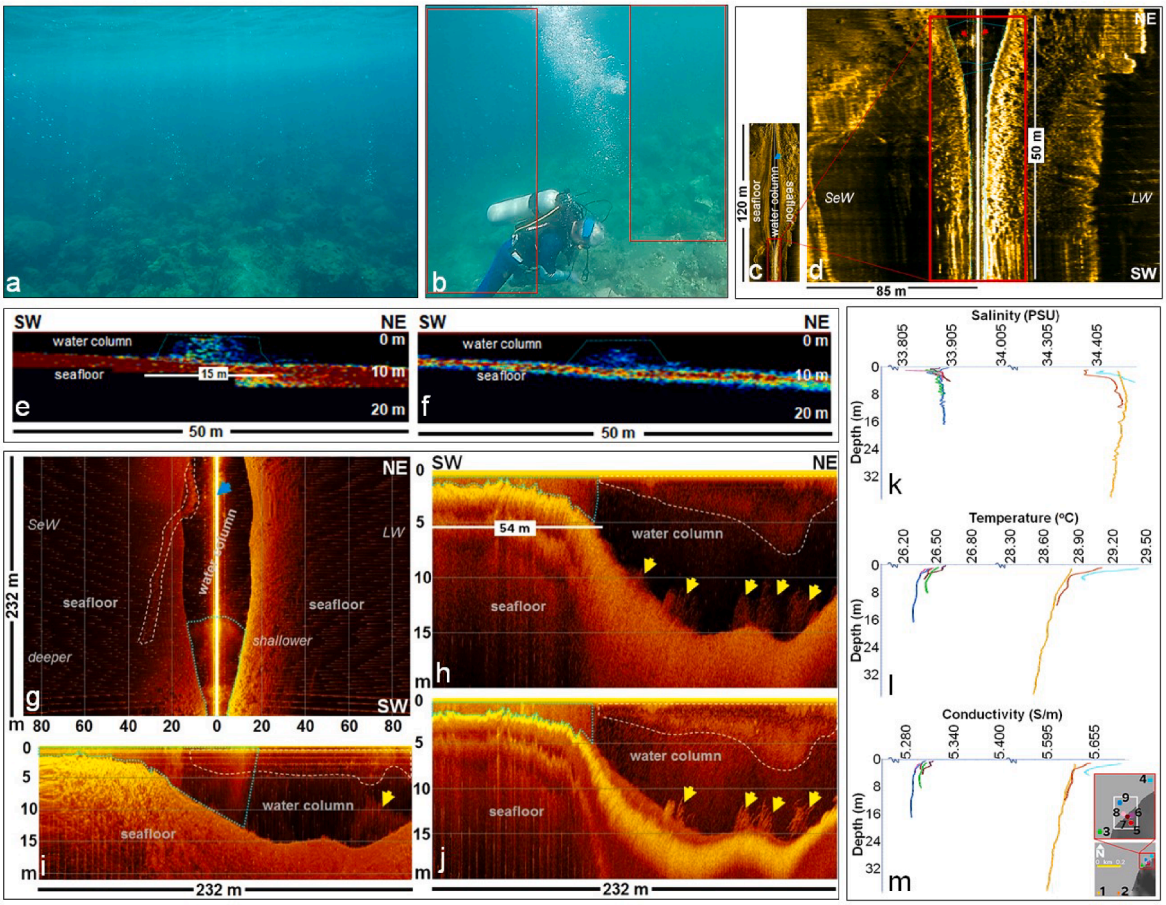

Fig. 4. Sparse-type SGD in Balayan Bay. (a) Frequent gas discharges at depth <5 m; (b) sporadic gas discharge (enclosed in red boxes) from depths of about 7 m to 8 m. (c) 120-m side scan sonar image acquired using RGSSS, showing the coralline seafloor, nadir zone or boat track (blue arrow), and the identified SGD; (d) Zoomed in view of the RGSSS image with SGD, enclosed by the blue broken lines; red arrows indicate transducer trail. Each side of the image has a slant range = 75 m. RGES sonar images with identified SGD enclosed by blue broken lines in all panels – Garmin: (e) 77 kHz, (f) 200 kHz; Humminbird: (g) side scan image (455 kHz), (h) down scan image (83 kHz), (i) down scan image (455 kHz), (j) down scan image (200 kHz). CTD profiles: (k) Salinity, (l) temperature, (m) conductivity. In (g), the blue arrow indicates the nadir zone or the transducer track. The white, broken lines outline the wake of the passing boat; yellow arrows indicate parts of benthos. (See description of SGD and other figures in text). SeW = seaward, LW = landward. (For interpretation of the references to color in this figure legend, the reader is referred to the web version of this article.)

during SCUBA diving in September 2018. For the MantaCam video, follow this link: https://tinyurl.com/tingloySGD. Fig. 5a shows a photograph of the spring-type, bubbly SGD plume emanating from a single point source at the rubbly and sandy seafloor, about 9 m deep. This intense degassing lies within a sparse-type SGD field.

SGD signature in the RGSSS images was seen in this location as less distinct, discrete acoustic anomalies in the water column, at depths of about 10 m (5b). Spring-type was seen as stronger signal, in contrast with the sparse-type SGD features in the area. Collectively, gas bubbles were imaged as a 50-m discrete near-seafloor feature (5c). Linear features on the seafloor where the SGD is emanating were identified as lineaments. This suggests that the intense discharge flow amid the rubble in this site can be fault-related. The image also shows rubble on the landward side, with sandier seaward side.

Following these results, sonar image acquired with the 77 kHz frequency of Garmin also shows good contrast between the spring- and sparse-type SGD features (5d). The spring-type has stronger signal with more intense yellow to red scattering, against the less distinct blue signal of sparse-type. In Fig. 5e, the rise velocity of both SGDs is estimated to be ranging from 25 cm/s at depth of about 9 m, to 45 cm/s at 4 m.

From the generated model for rising bubbles by McGinnis et al. (2006), ascending bubbles with 5 mm to 20 mm diameter must be rising at 20 cm/s to 30 cm/s, respectively. In this study, the bubble size, bubble composition (i.e., contaminants), pressure, and depth were the main factors affecting the rise velocities (McGinnis et al., 2006; Tassin and Nikitopoulos, 1995). Considering that the bubbly SGDs in the area are CO_2-rich and are emanating from sandy seafloors with high amount of possible solid and dissolved constituents (Cardenas et al., 2020), high level of interactions was possible, slowing down the small rising bubbles at the bottom (Tassin and Nikitopoulos, 1995).

In Humminbird, SGD features were more distinct in the down scan images of 83 kHz (5 g) and 200 kHz (5i). In all frequencies, suspended sediments reduced the signal contrast in the water column. Unlike the sonar images from other units, the sparse-type SGD is masking the spring-type in all Humminbird sonar images. While the linear features inferred as lineaments using RGSSS are also present in the RGES side scan sonar image (5f).

The identified spring-type bubbly SGD was further characterized by high temperature, low salinity, and low conductivity values. Salinity was decreasing with depth within the spring but slightly increasing outside (5j). Temperature within the spring was increasing near the point source, with decreasing trend outside bubble field (5k). And conductivity was significantly lower at the point source on the seafloor, slightly increasing towards the surface (5l). The results of CTD casting were interpreted as characteristics of a classic intense degassing in a geothermally active region. The fresher SGD output contributed to the significant variations of the measured parameters.

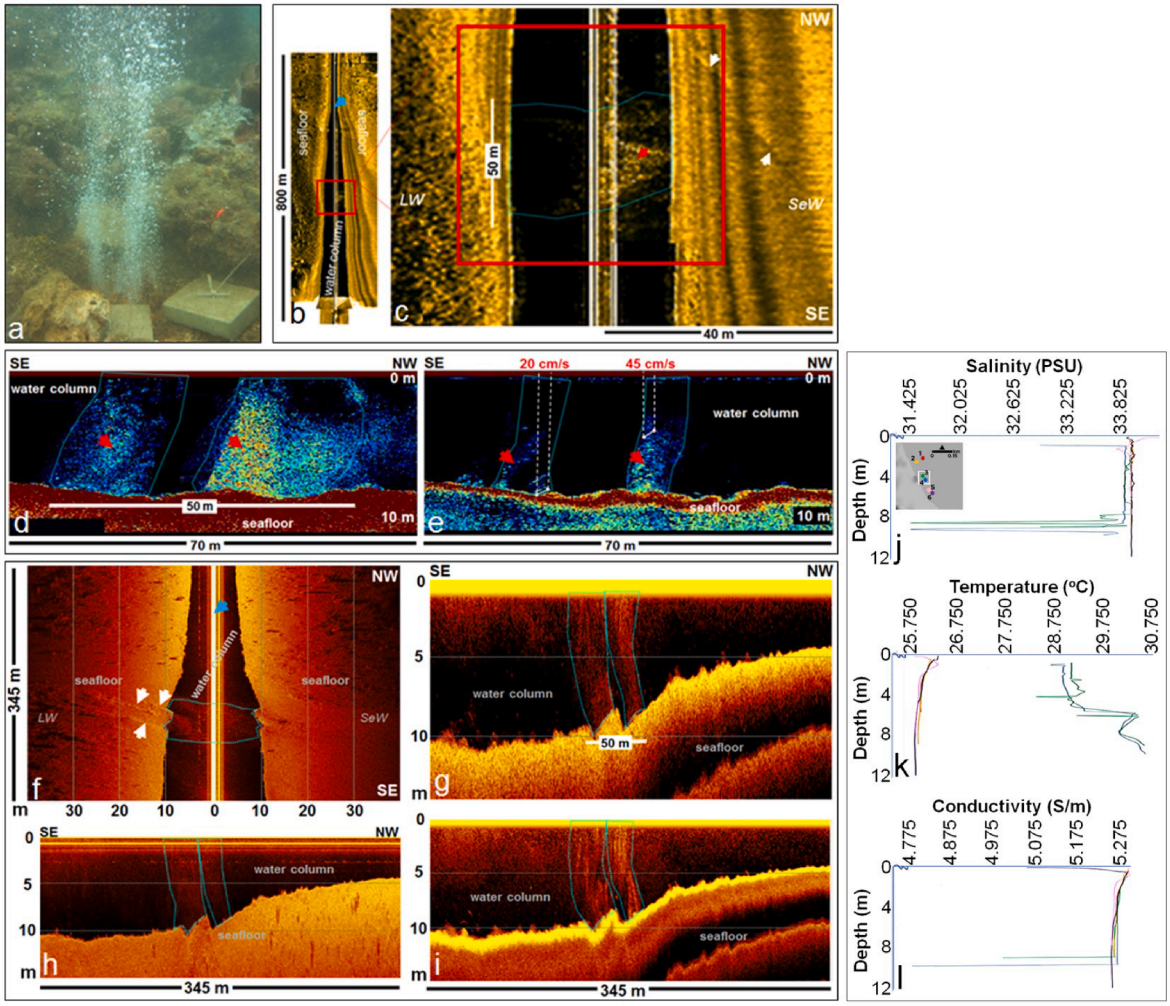

Fig. 5. Spring-type in sparse-type SGD field in Tingloy. (a) Spring-type SGD amidst the sparse-type SGD in Tingloy, at 9 m depth; (b) 800-m side scan sonar image acquired using RGSSS, nadir zone/boat rack indicated by blue arrow; (c) Zoomed in view of the sonar image with 50-m bubbly SGD field enclosed by the blue broken lines, spring-type SGD is indicated by the red arrow. Each side of the image in (b) has a slant range = 75 m. RGES sonar images, with identified SGD enclosed by blue broken lines in panels (d) – (i). Garmin: (d) 77 kHz, (e) 200 kHz; Humminbird: (f) side scan image (455 kHz), (g) down scan image (83 kHz), (h) down scan image (455 kHz), (i) down scan image (200 kHz). CTD profiles: (j) Salinity, (k) temperature, (l) conductivity. The identified bubbly SGD plumes are enclosed by the blue broken lines in (d) – (i), with the sparse-type masking the spring-type SGD. In (f), the blue arrow indicates the nadir zone or the transducer track. In (b) and (f), the white arrows indicate the inferred lineament. (See description of SGD and other features in text). SeW = seaward, LW = landward. (For interpretation of the references to color in this figure legend, the reader is referred to the web version of this article.)

3.3. Curtain-type

Towards the tip of Calumpan Peninsula in Batangas Bay (Fig. 2), SGD occurrence was more prevalent and extensive, forming a series of curtains of bubbles. Bubble Point, Soda Springs, and Mainit Point (Fig. 2) composed this well-documented curtain-type SGD in Batangas Bay (Cardenas et al, 2020).

Fig. 6a shows a MantaCam snapshot of dense and extensive bubbles emerging from depths of 2 m to 3 m. Fig. 6b shows the less frequent gas discharges at depth of about 5 m (enclosed by the red box). For more MantaCam videos, follow this link: https://tinyurl.com/batangasSGD.

The less frequent discharges at 5 m to 6 m were seen as series of more prominent, dispersed curtains of bubbles over a wide area using Garmin. In 77 kHz, the identified SGD features (6c) appear to have stronger signatures. Both frequencies imaged SGD signatures disappearing in mid-water, with >80% of the bubble percentage not being imaged in 200 kHz (6d). SGD features were seen rising to the sea surface at 10° to 20° inclination.

In the 200 kHz sonar image, bubble lines of the identified SGD features are well-defined. In this location, the rise velocities slightly vary from 30 cm/s at depth of about 6 m, to 35 cm/s at depth of about 3 m. These estimated velocities indicate that the rising bubbles in this area can expand bigger than 20 mm, since the values are slightly higher than the theoretical range (McGinnis et al., 2006).

Fig. 6e shows the ER distribution to sub-bottom depths of about 3 m to 24 m, with relatively high resistivity records (yellow to red color), which match parts of these curtains of bubbles. From the inversion, a slightly stronger mixed water signal (yellow-green to green) compared to the Balayan Bay ER data was derived. This is interpreted as a result of seawater recirculation. Thus, the discharge is mixed freshwater SGD and recirculated SGD.

Locations of the identified curtain-type SGD matched the areas with slightly low salinity (6h), elevated temperature (6i), and slightly higher conductivity (6j), with respect to ambient nearshore seawaters. The bottom salinity and conductivity within the bubble field are slightly lower than the ambient seawater. The bottom temperature is slightly elevated inside the bubble field. However, no significant variations were observed from the values (6h-6m), indicating the probable mixing of waters, further indicating the presence of recirculated SGD in the area.

To further assess the capability of an RGES, Fig. 6f and 6g show

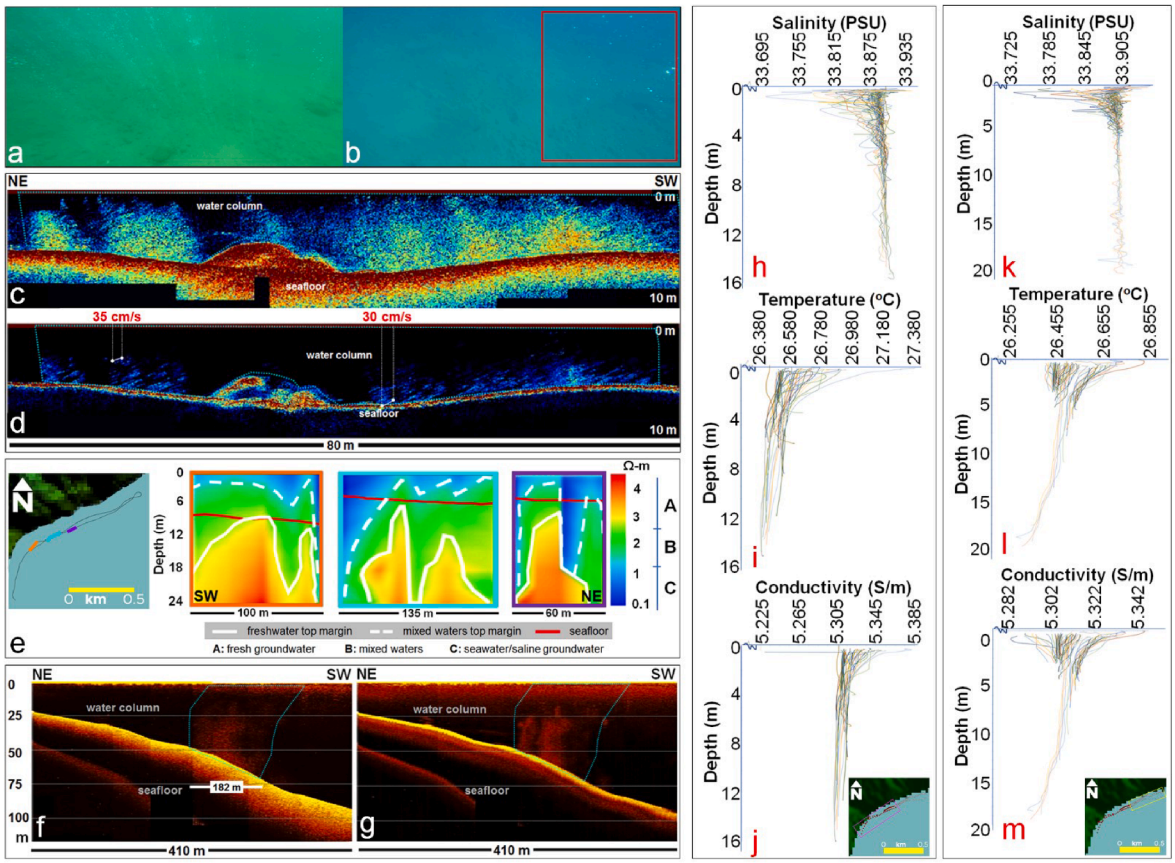

Fig. 6. Curtain-type SGD in Batangas Bay. MantaCam snapshots: (a) Dense and extensive bubbles emerging from depths ~ 2 m to 3 m, (b) less frequent gas discharges at depth ~ 5 m (enclosed by the red box). Garmin sonar images: (c) 77 kHz, (d) 200 kHz. (e) ER profile at depths 3 – 6 m matching locations of SGDs identified by Garmin. Location of the CRP survey lines (left – right) are indicated by the orange, cyan, and purple lines on the corresponding location map. Humminbird sonar images: (f) down scan image (83 kHz), (g) down scan image (200 kHz). The identified bubbly SGD plumes are enclosed by the blue broken lines in all RGES images. CTD profiles inside the bubble field: (h) Salinity, (i) temperature, (j) conductivity; outside the bubble field: (k) Salinity, (l) temperature, (m) conductivity. (See description of SGD and other figures in text). (For interpretation of the references to color in this figure legend, the reader is referred to the web version of this article.)

deeper-water SGD identified as part of the Soda Springs (Cardenas et al., 2020). However, the 455 kHz frequency failed to image the SGD features. Sonar images of the down scan show a 182-m curtain of bubbles. The signals disappeared at a depth of about 15 m, indicating bubble dissolving and incorporating with seawater. SGD features were seen emanating from the seafloor at 10° to 15° angle, with more tilting towards the sea surface. For more supporting information, Cardenas et al. (2020) has a compilation of video footages of their deep dive in Batangas Bay, confirming that the bubbles imaged in this location are indeed SGDs that are parts of Soda Springs.

3.4. Key findings (RGES)

Fig. 7 shows the locations of all nearshore SGD occurrence imaged using the RGES units. The blue lines correspond to the locations of SGD identified using the Humminbird with 83/200/455 kHz; pink lines are SGD fields identified using the Garmin unit with 77/200 kHz. The plots of transects with identified SGD signature were connected to generate the specific areas for ground truthing. SGD sites covering an area of 170,800 m^2 in Batangas Bay, 676 m^2 in the Balayan Bay, and 830 m^2 in the eastern coast of Tingloy were generated.

The results of this study show that gas bubbles indicating SGD occurrences exhibit acoustic anomalies in the water column that can be detected using the identified frequencies of RGES. This is due to the characteristics of small bubbles and freshwater discharges as effective scatterers and absorbers of sound waves; aided by the significantly high-density variation between seawater and gas discharge, and the acoustic resonance effect controlled by bubble size, sonar frequency, and water depth (Medwin and Clay, 1998; Nakamura et al., 2015). Similar SGD signatures were detected in approximately the same positions, further confirming that all frequencies used can effectively detect bubbly SGD.

However, although all sonar frequencies of both units imaged SGD signatures, the 77 kHz down scan frequency of Garmin and 83 kHz down scan frequency of Humminbird were the most effective in imaging bubbly discharges. Bubbles serve as good amplifiers of sonar signals, as the higher-limit resonance frequency (i.e., ~50 kHz) nearly matched the lowest frequencies (77 and 83 kHz). A small bubble resonates to sound whose wavelength is several hundred times its diameter that even a few and spatially distributed bubbles, which can be almost invisible, may show considerable acoustic anomalies (Spitzer, 1943). Given the high concentration of bubbles in SGD sites, the water column was seen as nearly acoustically opaque. Furthermore, lower frequencies have larger bottom coverage, imaging bigger areas and more features at a time. While the density of the rising bubbly discharge is controlled by its physico-chemical characteristics.

Considering the CO_2-rich composition and bubbly structure of SGD in the study sites (Cardenas et al., 2020), the curtains and plumes have higher acoustic contrast against the ambient water column. However, CO_2-rich bubbly SGD is thermodynamically unstable in seawater until it reaches certain depth where its density is equivalent to that of the ambient seawater (Nakamura et al., 2015). At this depth, the bubbly discharge expands horizontally, and dissolves into surrounding seawater

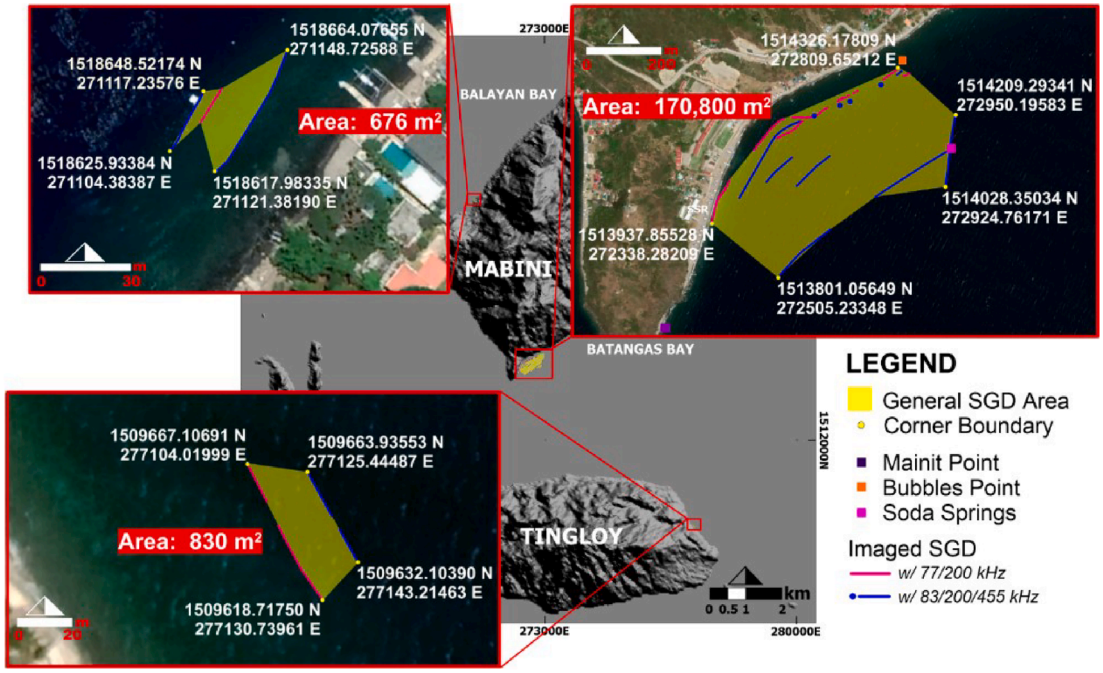

Fig. 7. SGD sites imaged using the RGES with different frequencies: blue lines are the locations of SGD imaged with 83/200/455 kHz; pink lines are identified using 77/200 kHz. Yellow polygons show the SGD areas in the surveyed sites. (For interpretation of the references to color in this figure legend, the reader is referred to the web version of this article.)

(Nakamura et al., 2015; Zhao et al., 2017). This is probably the reason why in Soda Springs, the bubbles were not observed at sea surface, and acoustic signatures immediately disappeared at 15-m depth (Fig. 6).

From the sonar images, RGES with fixed frequencies showed sharp acoustic signatures of sparse-, curtain-, and spring-type SGD in shallow nearshore waters (<2 m to ~75 m) in the hydrothermal areas of Mabini and Tingloy, Batangas. Specifically, sonar images in all sites showed that the acoustic signatures of bubbly SGD can be indicated by near-seafloor to mid-water cloud- and curtain-like features.

The discrete, sparse-type SGD in Balayan Bay was observed as isolated vertically rising feature over a limited area. This feature does not seem to vary in width and general appearance across the water column. Acoustic signal of this type of bubbly SGD is weaker and more distributed than the spring-type.

The dispersed, curtain-like features in Batangas Bay showed more variation depending on the depth. Shallow discharges were seen as continuous near-seafloor or mid-water, curtain-like features with identifiable plumes at some parts.

SGDs in deeper waters (i.e., Soda Springs) were seen as cloud-like features with funnel morphology that dissipate in mid-water. Curtain-type may be composed of series of spring- and sparse-type SGDs, forming a chain of SGD signal over a wide area.

Discrete, spring-type SGD formed strong signatures of cloud-like features, also with an overall funnel-shaped morphology. This morphology is probably due to greater horizontal dispersion and expansion of bubbles as they migrate upwards. Spring-type SGD emanates from a single point source at the seafloor. Table 1 summarizes the comparison of these types based on their acoustic behavior and spatial distribution.

Sonar images also showed that RGES units have a good range of frequencies to detect other features that are not visible to other frequencies, or, in some cases, are visible to frequencies used in RGSSS units such as benthos on the seafloor, and suspended sediments and wake of the boat in the water column.

Table 1
SGD types based on their acoustic behavior and spatial distribution.

Acoustic Criteria	TYPES OF BUBBLY SGD		
	Spring	Sparse	Curtain
Extent of acoustic signal over an area	<10 m wide within at least a 100-m segment	>10 m; Sporadically-distributed within at least a 100-m segment	Continuous and widespread within at least a 100-m segment
Flow morphology/ geometry	Funnel-shaped	Vertical/inclined, no significant change in geometry	Varies depending on the dominant flow and depth
Density of signal	Intense/strong	Weak to moderate	Weak to strong
Brightness	Brightest at the center of plume	Moderate level, increasing towards the center of cloud	Almost uniform throughout
Point source	Mostly single point	Over a specific area	Over an extended area

4. Conclusions

Local studies focusing only on mapping and characterizing SGD occurrence is scarce. This is mainly because currently utilized methods are tedious, costly, and mostly require site-specific assessments over a wide range of spatial scales and/or delicate geochemical procedures. To date, the most used on-ground methods in mapping SGD occurrences in the Philippines include CRP, continuous Radon in water, and SCUBA diving.

Use of sonar systems in detecting features similar to SGD occurrences was explored in recent years (Nakamura et al., 2015; Greinert, 2008; Hernández et al., 2017; McGinnis et al., 2006; Zhao et al., 2017), but there were no published materials looking at the utility of RGES in mapping and imaging SGD occurrences. In this study, the utility of RGES was evaluated and is assessed as a good tool for mapping bubbly coastal SGDs.

Using the developed approach, the RGES successfully imaged, identified, and characterized nearshore and shallow-water bubbly SGDs,

and their corresponding point sources in the three survey areas. The results further show that although all frequencies of the RGES used can image SGD occurrence, 77 and 83 kHz down scan frequencies are the most effective. Sonar images acquired with these frequencies showed clearer acoustic signatures and more accurate point source locations of the different types of bubbly coastal SGD.

Finally, cluster of bubbles or gas discharges have higher backscatter strength than the noise in the water column. Hence, can be found by manual detection from sonar images. Although manual detection can be variable due to subjective differences in experience and amount of sonar images to be interpreted, it is also definitive and convenient.

5. Recommendations

Further research can be conducted in areas with known SGD discharges without bubbles to test the capability of RGES in imaging water-dominated discharges with varying temperature and salinity conditions. This recommendation follows that of Artemov (2006), who mentioned that the flares observed in sonar images may also indicate less dense water bodies. The imaging capability of other frequencies, if available in other RGES models, can be evaluated. At present, the most common combination of frequencies of available RGES is 50–85/200 kHz. Lastly, RGES is highly recommended as a mapping tool in preliminary surveys for nearshore bubbly SGD-related research such as in areas with shallow hydrothermal vents and methane emanations.

CRediT authorship contribution statement

Mary Rose P. Gabuyo: Conceptualization, Methodology, Software, Validation, Investigation, Formal analysis, Investigation, Data curation, Writing – original draft, Writing – review & editing, Visualization, Funding acquisition. **Fernando P. Siringan:** Conceptualization, Methodology, Investigation, Resources, Writing – review & editing, Supervision, Project administration, Funding acquisition.

Declaration of Competing Interest

The authors declare that they have no known competing financial interests or personal relationships that could have appeared to influence the work reported in this paper.

Acknowledgment

Funding: This work was supported in part by the Department of Science and Technology - Philippine Council for Industry, Energy, and Emerging Technology Research and Development (DOST-PCIEERD) through the “Mapping of Active Offshore Faults for Resilient Coasts Project;” and the Department of Science and Technology - Science Education Institute (DOST-SEI) through the “Accelerated Science and Technology Human Resource Development Program.” The authors thank Keanu Sarmiento, Paul Flores, Edwin Dumalagan, Jr., Angel Doctor, and Denise Janer for joining the coastal dives; Raymond Rodolfo for his invaluable input on the Soda Springs data analysis; and Dr. William Burnett for allowing the use and modification of the image for the definition of SGD.

References

Artemov, Y.G., 2006. Software support for investigation of natural methane seeps by hydroacoustic method. Mar. Ecol. J. 5, 57–71.

Baraza, J., Ercilla, G., 1996. Gas-charged sediments and large pockmark-like features on the Gulf of Cadiz slope (SW Spain). Mar. Pet. Geol. 13 (2), 253–261. https://doi.org/10.1016/0264-8172(95)00058-5.

Blondel, P., 2009. The Handbook of Sidescan Sonar. Praxis Publishing Ltd., Chichester, UK.

Burnett, W.C., Taniguchi, M., Oberdorfer, J., 2001. Measurement and significance of the direct discharge of groundwater into the coastal zone. J. Sea Res. 46 (2), 109–116. https://doi.org/10.1016/S1385-1101(01)00075-2.

Burnett, W.C., Bokuniewicz, H., Huettel, M., Moore, W., Taniguchi, M., 2003. Groundwater and pore water inputs to the coastal zone. Biogeochem. 66 (1/2), 3–33. https://doi.org/10.1023/B:BIOG.0000006066.21240.53.

Burnett, W.C., Aggarwal, P.K., Aureli, A., Bokuniewicz, H., Cable, J.E., Charette, M.A., Kontar, E., Krupa, S., Kulkarni, K.M., Loveless, A., Moore, W.S., Oberdorfer, J.A., Oliveira, J., Ozyurt, N., Povinec, P., Privitera, A.M.G., Rajar, R., Ramessur, R.T., Scholten, J., Stieglitz, T., Taniguchi, M., Turner, J.V., 2006. Quantifying submarine groundwater discharge in the coastal zone via multiple methods. Sci. Total Environ. 367 (2-3), 498–543. https://doi.org/10.1016/j.scitotenv.2006.05.009.

Cantarero, D.L.M., Blanco, A., Cardenas, M.B., Nadaoka, K., Siringan, F.P., 2019. Offshore submarine groundwater discharge (SGD) at a coral reef front controlled by faults. Geochem., Geophys., Geosyst. 20 https://doi.org/10.1029/2019gc008310.

Cardenas, M.B., Rodolfo, R.S., Lapus, M.R., Cabria, H.B., Fullon, J., Gojunco, G.R., Breecker, D.O., Cantarero, D.M., Evaristo, J., Siringan, F.P., Zhang, T., 2020. Submarine groundwater and vent discharge in a volcanic area associated with coastal acidification. Geophys. Res. Lett. 47 (1) https://doi.org/10.1029/2019GL085730.

Carpenter, K.E., Springer, V.G., 2005. The center of the center of marine shore fish biodiversity: the Philippine Islands. Environ. Biol. Fish. 72 (4), 467–480. https://doi.org/10.1007/s10641-004-3154-4.

Del Rosario, R.A., Jr., Oanes, A.F., 2010. Controlled source magnetotelluric survey of Mabini Geothermal Prospect, Mabini, Batangas, Philippines, in: Proceedings World Geothermal Congress 2010. Bali, IDN.

Fondriest Environmental, Inc. (FEI), 2014. Conductivity, Salinity and Total Dissolved Solids. Fundamentals of Environmental Measurements (WWW Document). Fondriest Environmental, Inc. URL https://www.fondriest.com/environmental-measurements/parameters/water-quality/conductivity-salinity-tds/ (accessed 10.05.20).

Garmin, 2016. GPSMAP® 500/700 Series and echoMAP™ 50/70 Series: Owner’s Manual. Garmin Ltd., Schaffhausen, CH.

Greinert, J., 2008. Monitoring temporal variability of bubble release at seeps: The hydroacoustic swath system GasQuant. J. Geophys. Res. 113 (C7) https://doi.org/10.1029/2007JC004704.

Hernández, P.A., Melián, G.V., Somoza, L., Arpa, M.C., Pérez, N.M., Bariso, E., Sumino, H., Padrón, E., Varekamp, J.C., Albert-Beltran, J., Solidum, R., 2017. The acid crater lake of Taal Volcano, Philippines: hydrogeochemical and hydroacoustic data related to the 2010–11 volcanic unrest. Geol. Soc. Lond. Spec. Publ. 437 (1), 131–152. https://doi.org/10.1144/SP437.17.

Homestead, 2017. Cone Angles [WWW Document]. Homestead. URL https://learnside imaging.homestead.com/sonar.html (accessed 11 110 20).

Horigue, V., Y. licuanan, W., 2013. Sensitivities of coral reefs in the Verde Island Passage to climate change. Galaxea J. Coral Reef Stud. 15 (Supplement), 359–365. https://doi.org/10.3755/galaxea.15.359.

Humminbird, 2013. 698ci HD SI Combo Operations Manual. Johnson Outdoors Marine Electronics, Alpharetta, GA, USA.

Idczak, J., Brodecke – Goluch, A., Lukawska – Matuszewska, K., Graca, B., Gorska, N., Klusek, Z., Pezacki, P., Bolalek, J., 2020. A geophysical geochemical and microbiological study of a ewly discovered pockmark with active gas seepage and submarine groundwater discharge (MET1-BH, central Gulf of Gdańsk, southern Baltic Sea. Sci. Total Environ. 742, 140306. doi:10.1016/j.scitotenv.2020.140306.

Johannes, R.E., 1980. The ecological significance of the Submarine Discharge of Groundwater. Mar. Ecol. Prog. Ser. 3, 365–373. https://doi.org/10.3354/meps003365.

Judilla, R.J., Jauod, J., Capili, E., Jr., Soriano, M., 2012. Teardrop – a rapid reef mosaicking tool for coastal communities, in: Proceedings of the 12th International Coral Reef Symposium. Cairns, AUS.

Kang, K.-M., Kim, D.-J., Kim, Y., Lee, E., Kim, B.-G., Kim, S.H., Ha, K., Koh, D.-C., Cho, Y.-K., Kim, G., 2019. Quantitative estimation of submarine groundwater discharge using airborne thermal infrared data acquired at two different tidal heights. Hydrol. Process. 33 (7), 1089–1100. https://doi.org/10.1002/hyp.13387.

Kingon, K., 2013. Mapping, Classification, and Spatial Variation of Hardbottom Habitats in the Northeastern Gulf of Mexico. Florida State University, Florida, USA. Doctoral dissertation.

McCartney, B.S., Bary, B.M., 1965. Echo-sounding on probable gas bubbles from the bottom of Saanich Inlet, British Columbia. Deep Sea Res. Oceanogr. Abstr. 12 (3), 285–294. https://doi.org/10.1016/0011-7471(65)90002-1.

McGinnis, D.F., Greinert, J., Artemov, Y., Beaubien, S.E., Wüest, A., 2006. Fate of rising methane bubbles in stratified waters: how much methane reaches the atmosphere? J. Geophys. Res. 111 (C9) https://doi.org/10.1029/2005JC003183.

Medwin, H., Clay, C.S., 1998. In: Fundamentals of Acoustical Oceanography. Academic Press, San Diego, CA, USA. https://doi.org/10.1016/B978-0-12-487570-8.X5000-4.

Mitchell, G., Gharib, J.J., Millar, D.R., 2017. Deepwater Hydrocarbon Seep Detection: Tools and Techniques using Multibeam Echo sounders, in: U.S. Hydro 2017. Houston, TX, USA.

Moore, W.S., 2010. The effect of submarine groundwater discharge on the ocean. Annu. Rev. Mar. Sci. 2 (1), 59–88. https://doi.org/10.1146/annurev-marine-120308-081019.

Moosdorf, N., Stieglitz, T., Waska, H., Dürr, H.H., Hartmann, J., 2015. Submarine groundwater discharge from tropical islands: a reviewSubmariner Grundwasserabfluss von tropischen Inseln – Ein Review. Groundwasser 20 (1), 53–67. https://doi.org/10.1007/s00767-014-0275-3.

Mulligan, E., Charette, M.A., Tamborski, J.J., Moosdorf, N., 2019. Submarine Groundwater Discharge. In: Reference Module in Earth Systems and Environmental Sciences. Elsevier, Netherlands, pp. 108–119.

Nakamura, K., Kawagucci, S., Kitada, K., Kumagai, H., Takai, K., Okino, K., 2015. Water column imaging with multibeam echo-sounding in the mid-Okinawa Trough: Implications for distribution of deep-sea hydrothermal vent sites and the cause of

acoustic water column anomaly. Geochem. J. 49 (6), 579–596. https://doi.org/10.2343/geochemj.2.0387.

National Oceanic and Atmospheric Administration (NOAA), 2019. What is bathymetry? [WWW Document]. NOAA. URL https://oceanservice.noaa.gov/facts/bathymetry.html (accessed 01.20.20).

Prakash, R., Srinivasamoorthy, K., Gopinath, S., Saravanan, K., 2018. Measurement of submarine groundwater discharge using diverse methods in Coleroon Estuary, Tamil Nadu, India. Appl. Water Sci. 8 (1) https://doi.org/10.1007/s13201-018-0659-0.

Rodolfo, R.S., 2019. Characterization of submarine groundwater discharge in Mabini, Batangas: Linking geology, submarine groundwater discharge and coastal ecosystems. Ateneo de Manila University, Quezon City, PH. Master's Thesis.

Senal, M.I.S., Jacinto, G.S., San Diego-McGlone, M.L., Siringan, F., Zamora, P., Soria, L., Cardenas, M.B., Villanoy, C., Cabrera, O., 2011. Nutrient inputs from submarine groundwater discharge on the Santiago reef flat, Bolinao, Northwestern Philippines. Mar. Pollut. Bull. 63 (5-12), 195–200. https://doi.org/10.1016/j.marpolbul.2011.05.037.

Spitzer, Jr., L., 1943. Acoustic properties of gas bubbles in a liquid. Unclassified report prepared for U.S. Government. Office of Scientific Research and Development. Ohio: Document Service Center, Ohio.

Szymczycha B., Pempkowiak J., 2016. State of Art and Theory of Submarine Groundwater Discharge (SGD), in: The Role of Submarine Groundwater Discharge as Material Source to the Baltic Sea (3-32). GeoPlanet: Earth and Planetary Sciences. Springer, Cham. DOI: 10.1007/978-3-319-25960-4_2.

Taniguchi, M., Burnett, W.C., Cable, J.E., Turner, J.V., 2002. Investigation of submarine groundwater discharge. Hydrol. Process. 16 (11), 2115–2129. https://doi.org/10.1002/hyp.1145.

Taniguchi, M., Ishitobi, T., Shimada, J., 2006. Dynamics of submarine groundwater discharge and freshwater-seawater interface. J. Geophys. Res. 111 (C1) https://doi.org/10.1029/2005JC002924.

Taniguchi, M., Dulai, H., Burnett, K.M., Santos, I.R., Sugimoto, R., Stieglitz, T., Kim, G., Moosdorf, N., Burnett, W.C., 2019. Submarine groundwater discharge: Updates on its measurement techniques, geophysical drivers, magnitudes, and effects. Front. Environ. Sci. 7 https://doi.org/10.3389/fenvs.2019.00141.

Tassin, A.L., Nikitopoulos, D.E., 1995. Non-intrusive measurements of bubble size and velocity. Exp. Fluids 19 (2), 121–132. https://doi.org/10.1007/BF00193858.

The MarineBio Conservation Society (TMCS), 2019. Ocean and Temperature [WWW Document]. TMCS. URL https://marinebio.org/oceans/temperature/ (accessed 10.05.20).

Tsai, C.-H., Hsu, S.-K., Lin, S.-S., Yang, T.F., Wang, S.-Y., Doo, W.-B., Lee, H.-F., Lan, T., Huang, J.-C., Liang, C.-W., 2017. The Keelung Submarine Volcano in the near-shore area of northern Taiwan and its tectonic implication. J. Asian Earth Sci. 135, 320–326. https://doi.org/10.1016/j.jseaes.2016.12.041.

United Nations Educational, Scientific and Cultural Organization (UNESCO), 2004. Submarine groundwater discharge: Management implication, measurements, and effects (SC.2004/WS/4). United Nations Educational, Scientific and Cultural Organization, Paris.

Zhao, J., Wang, X., Zhang, H., Wang, A., Zhao, J., Wang, X., Zhang, H., Wang, A., 2017. A Comprehensive Bottom-Tracking Method for Sidescan Sonar Image Influenced by Complicated Measuring Environment. IEEE J. Ocean. Eng. 42, 619–631. https://doi.org/10.1109/JOE.2016.2602642.